Hyper-Laplacian Regularized Unidirectional Low-rank Tensor Recovery for Multispectral Image Denoising

Yi Chang, Luxin Yan*, Sheng Zhong

National Key Laboratory of Science and Technology on Multispectral Information Processing
School of Automation, Huazhong University of Science and Technology, China

{yichang, yanluxin, zhongsheng}@hust.edu.cn

Abstract

Recent low-rank based matrix/tensor recovery methods have been widely explored in multispectral images (MSI) denoising. These methods, however, ignore the difference of the intrinsic structure correlation along spatial sparsity, spectral correlation and non-local self-similarity mode. In this paper, we go further by giving a detailed analysis about the rank properties both in matrix and tensor cases, and figure out the non-local self-similarity is the key ingredient, while the low-rank assumption of others may not hold. This motivates us to design a simple yet effective unidirectional low-rank tensor recovery model that is capable of truthfully capturing the intrinsic structure correlation with reduced computational burden. However, the low-rank models suffer from the ringing artifacts, due to the aggregation of over-lapped patches/cubics. While previous methods resort to spatial information, we offer a new perspective by utilizing the exclusively spectral information in MSIs to address the issue. The analysis-based hyper-Laplacian prior is introduced to model the global spectral structures, so as to indirectly alleviate the ringing artifacts in spatial domain. The advantages of the proposed method over the existing ones are multi-fold: more reasonably structure correlation representability, less processing time, and less artifacts in the overlapped regions. The proposed method is extensively evaluated on several benchmarks, and significantly outper-forms state-of-the-art MSI denoising methods.

1. Introduction

A MSI could provide abundant information with multiple specific frequencies across the electromagnetic spectrum, which facilitates the fine representation of a real scene. Unfortunately, during the imaging procedure, the MSI is usually contaminated by the noises, e.g., Gaussian noise, making the MSI unsuitable for subsequent applications. Therefore, denoising has been an essential prepro-

cessing step for further MSI applications, such as classification [33], super-resolution [6], compressive sensing [31].

In MSI denoising, the non-local self-similarity which has been widely used in single image processing, and the additional high spectral correlation have been extensively proven to be efficient prior knowledge [10, 11, 32]. The low-rank tensor models [21, 34, 7] have been proposed to exploit the two kinds of knowledge simultaneously by constructing a 3-order tensor, namely the spatial local sparsity (mode-1), non-local self-similarity (mode-2), and spectral high correlation (mode-3). Generally, most of existing low-rank tensor models utilize these knowledge by simply adding up the ranks (or its relaxations) along all tensor modes [24, 16, 9, 26]. A major difference with the matrix case, however, is the fact that the different n-ranks of a higher-order tensor are not necessarily the same [15]. It is unreasonable for previous works to ignore the subspace discrepancy among each mode.

The ISTReg was proposed very recently [26] by taking both fine-grained tensor sparsity insights of Tucker and CANDECOMP/PARAFAC (CP) low-rank decompositions into consideration to capture intrinsic structure correlation among each mode. The intuition behind ISTReg is to add more constraints into the model. However, this makes the heavy computational burden issue more unacceptable, which naturally exists in MSI due to its large volume. Our starting point to capture intrinsic structure correlation is in line with ISTReg [26], while we take a step from the opposite philosophy by distinguishing subspace discrepancy among each mode. Specifically, we intend to utilize the key structure correlation and discard the weaker correlation, so as to obtain the better result in a reasonable time.

To this end, we firstly illustrate why low-rank tensor recovery model performs better than the low-rank matrix recovery model in multispectral images and then give a detailed analysis about the rank properties along each mode of the constructed 3-order tensor via the high-order singular value decomposition (HOSVD). We discover that low-rank property of the non-local self-similarity is significantly su-

perior to that of the spatial and spectral correlation. Motivated by this observation, a simple yet effective unidirectional low-rank tensor prior is proposed to model the intrinsic correlation of the MSI in a more reasonable manner with less processing time.

Although patch/cubic based low-rank methods obtain state-of-the-art performance, they inevitably introduce the consistency issue of the overlapped pixels due to the patch/cubic aggregation operation. Conventional methods usually handle this problem from the spatial view [35, 13]. We offer a new perspective from the exclusively spectral correlation in MSI to alleviate this problem. We benefit from additional spectral information and model it with analysis-based hyper-Laplacian prior, which is free of patch partition operation. Integrating an analysis-based hyper-Laplacian prior into synthesis-based low-rank tensor model can reduce the ringing artifacts in spatial domain meanwhile better preserve the spectral structure. At last, we develop an efficient optimization algorithm to solve the proposed hyper-**L**aplacian regularized unidirectional **l**ow-**r**ank **t**ensor recovery problem (LLRT).

The contributions of this paper include: 1) The detailed low-rank property of MSI is explored in both matrix and tensor cases, which offers a new insight to model the low-rank property in MSI. A unidirectional low-rank tensor recovery model is proposed for accurate and fast encoding the intrinsic low-rank property of a MSI; 2) The hyper-Laplacian prior is introduced to model the consistency issue from the spectral perspective. On one hand, the spatial inconsistency pixels can be suppressed; on the other hand, the spectral structure can be well preserved; 3) We develop an efficient optimization scheme for LLRT minimization. The proposed method has been tested on extensive MSI datasets. The results validate that LLRT outperforms state-of-the-art methods by a large marginal in terms of both performance and speed.

2. Related work

Low-rank matrix/tensor recovery is a representative kind of state-of-the-art MSI denoising method. We compare them with proposed method in three important aspects.

Information Utilization: The spectral correlation and non-local self-similarity are two intrinsic characteristics underlying a MSI. Early methods usually utilized one of them [5, 19, 30, 27], which may obtain a suboptimal result. Peng *et al.* [21] firstly modeled them simultaneously, and more sophisticated methods have been proposed [16, 10, 7, 26, 32]. Our work follows this line. We suggest that while the information is indeed helpful, the key to the final performance depends heavily on how we reasonably model it.

Low-rank Modeling: For the information modeling, most of previous low-rank models regularized the sum of the rank

along each mode of the constructed tensor [24, 16, 9, 26]. It is unreasonable to equally enforce low-rank constraint along each mode, where the rank along each mode has clear physical meanings and should be treated differently. Moreover, these low-rank based methods suffer from the consistency issue due to patch/cubic aggregation.

In this work, we argue that the low-rank property of the non-local self-similarity is much more superior to that of the others (section 3.2). And we introduce the patch-free analysis prior from the spectral perspective to model the consistency issue (section 3.4). We seek to design a unified framework to jointly utilize the spectral and non-local similarity information from mutually complementary priors.

Running Time: The running time is closely related to the model, optimization, and implementation tricks. Due to the large size of MSI, the running time for previous low-rank tensor methods is usually long [16, 26]. We propose a simple yet effective model (section 3.4) with efficient optimization strategies (section 3.5) to reduce the running time.

3. Hyper-Laplacian regularized unidirectional low-rank tensor recovery model

3.1. Notations and preliminaries

In this paper, we denote tensors by boldface Euler script letters, e.g., $\boldsymbol{\mathcal{X}}$. Matrices are represented as boldface capital letters, e.g., $\boldsymbol{X}$; vectors are expressed with boldface lowercase letters, e.g., $\boldsymbol{x}$, and scalars are denoted by lowercase letters, e.g., x. The i-th entry of a vector $\boldsymbol{x}$ is denoted by x_i, element (i, j) of a matrix $\boldsymbol{X}$ is denoted by x_{ij}, and element (i, j, k) of a 3-order tensor $\boldsymbol{\mathcal{X}}$ is denoted by x_{ijk}. The *Frobenius* norm of an N-order tensor $\boldsymbol{\mathcal{X}} \in \mathbb{R}^{I_1 \times I_2 \times \cdots \times I_N}$ is the square root of the sum of the squares of all its elements, i.e., $\|\boldsymbol{\mathcal{X}}\|_F = \sqrt{\sum_{i_1=1}^{I_1} \sum_{i_2=1}^{I_2} \cdots \sum_{i_N=1}^{I_N} x_{i_1 i_2 \cdots i_N}^2}$. Tensor matricization, also named as *unfolding or flattening*, is the process of reordering the elements of an N-order tensor into a matrix. The mode-n matricization $\boldsymbol{X}^{(n)} \in \mathbb{R}^{I_n \times (I_1 \cdots I_{n-1} I_n \cdots I_N)}$ of a tensor $\boldsymbol{\mathcal{X}} \in \mathbb{R}^{I_1 \times I_2 \times \cdots \times I_N}$ is obtained by taking all the mode-n fibers to be the columns of the resulting matrix. Thus, the n-rank of a given tensor can be analyzed by means of matrix techniques. The rank of the matrix unfolding $\boldsymbol{X}^{(n)}$ is equal to the n-rank of $\boldsymbol{\mathcal{X}}$, i.e., $rank_n(\boldsymbol{\mathcal{X}}) = rank(\boldsymbol{X}^{(n)})$ [15].

3.2. Low-rank property in MSI

3.2.1 Limitation of the low-rank matrix model

In this section, we first illustrate why low-rank tensor recovery model performs better than low-rank matrix recovery model in MSI. As shown in Fig. 1, we provide three representative examples to point out that low-rank matrix recovery models for MSI denoising usually suffer from a problem: The obtained singular values are overshrunk, which
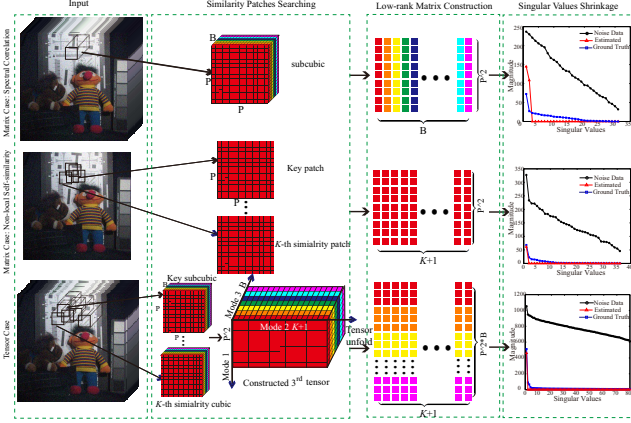
Figure 1. Low-rank property comparison between matrix and tensor. The first and second row illustrate the flowchart of spectral and non-local self-similarity based low-rank matrix case, respectively. The third row shows the flowchart of the unified low-rank tensor case. The last column illustrates the corresponding singular value sparsity and the overshrunk issue.

leads to a suboptimal solution.

To illustrate this, we applied the singular value decomposition (SVD) on the constructed matrixes to analyze the sparsity of the singular values of the clean image. We can observe that the percentage of non-zero element of the singular values in the tensor case is much less (blue), indicating that the intrinsic low-rank property of the constructed tensor is superior to that of the matrix cases. Then, we carried out an experiment by applying the singular value thresholding [1] on the singular value of noisy constructed matrixes (black) to discover how the estimated singular values (red) distribute compared with the oracle (blue).

One can see that the estimated singular values of matrix are deviated far from the oracle, especially in the spectral correlation case, meaning that the overshrinkage is serious. On the contrary, for the tensor case, the estimated singular values are more similar to the oracle. Moreover, the tensor format offers a unified understanding for the matrix-based recovery model. When $B = 0$ or $K = 0$, the constructed tensor degenerates into a matrix by taking only non-local self-similarity or spectral correlation. These phenomena motivate us to leverage the sparsity in tensor format for MSI denoising.

3.2.2 Closer Look at the low-rank property of tensor

In conventional tensor sparsity measures, they extended the 2-order sparsity measure to higher-order case by simply adding up rank along each modes. However, they neglected a fact that the different n-ranks of a higher-order tensor are not necessarily the same, indicating that the rank of each mode is closely related to its intrinsic low-rank subspace.
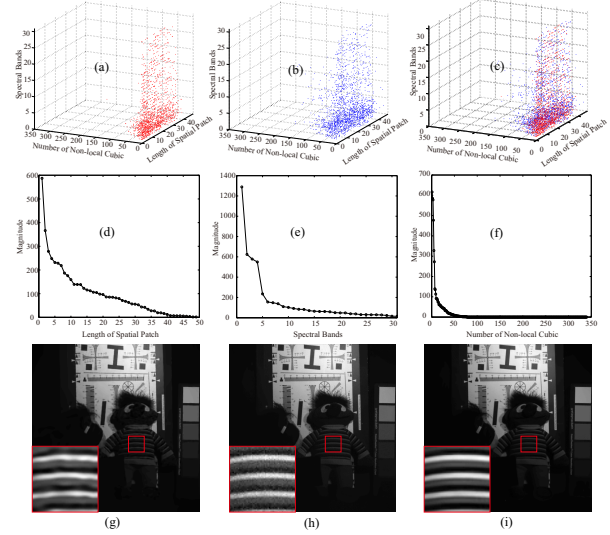

Figure 2. Low-rank property analysis of the constructed 3-order tensor along each mode via HOSVD. (a)-(i) is the visualization of singular values bigger than 1.5, bigger than 1 and smaller than 1.5, and overall bigger than 1 elements in the core tensor, respectively. (d)-(f) is the mean profile of (c) across spatial, spectral, and non-local self-similarity mode, respectively. (g)-(i) is the corresponding denoising result via spatial, spectral, and non-local self-similarity based low-rank tensor model, respectively.

To understand this, we explore the low-rank property of each mode of a constructed 3-order tensor $\mathcal{X}_i \in \mathbb{R}^{49 \times 350 \times 31}$ via HOSVD. We performed this experiment on hundreds tensor, and chose one as a representative. In Fig. 2(a)-(c), we give a visual understanding how the singular values distribute in the core tensor. Note that, most of small singular values are trivial. We just choose the larger singular values as representative, which are generally associated with the major projection orientations. In Fig. 2(d)-(f), we show the mean profile of the core tensor across each mode[1].

It is clearly observed that singular values of the core tensor exhibit significant sparsity with different degrees along each mode. Along the non-local self-similarity mode (mode-2), due to the strong redundancy of the non-local cubics, the coefficients tend to be decreasing extremely fast to zeroes. While along the spatial and spectral mode, albeit still approximately decreasing along the mode, most of the coefficients are non-zeros. Consequently, the corresponding denoising results are shown in Fig. 2(g)-(i). The result obtained by unfolding along the non-local self-similarity mode is much better than the others, since the sparser representation allow the most improvement [2].

The observation in Fig. 2 has truthfully reflected the intrinsic difference of structure correlation along each mode. The strong correlation across non-local self-similarity mode

---

[1]We slightly reordered the coefficients to be monotonically decreasing for better visualization, while this does not change the sparsity.
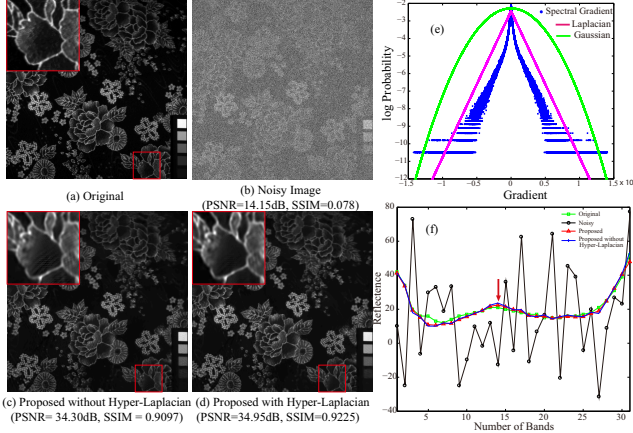
Figure 3. Effectiveness of spectral hyper-Laplacian prior in terms of suppressing the ringing artifacts and preserving spectral geometric structure. (a) Original image; (b) Simulated noisy image; (c) Restored result without hyper-Laplacian; (d) Restored result with hyper-Laplacian; (e) Fitting curves to the empirical distribution of spectral gradients; (f) Spectral reflectance at one location.

guarantees the low-rank property, while the subspaces along the other modes may not be low-rank, especially when it meets spectral inconsistency (mode-3) or spatial texture area (mode-1). Therefore, we argue non-local self-similarity is the key property contributing to MSI denoising performance, and should treat the rank along each mode differently.

3.3. Unidirectional low-rank tensor recovery

The analysis above reveals that the structure correlation along the non-local self-similarity mode is much stronger than the spatial or spectral mode. The conventional low-rank-based tensor recovery models that simply add up the rank along each mode ignored the difference of the structure correlation along each mode. Incorporating these weaker correlations across spatial mode at high frequency local region or across spectral mode with low spectral similarity, where the low-rank assumption cannot be met, may unexpectedly result in poor denoising results. Consequently, the truthful information recovered via non-local self-similarity mode may be lost, due to the aggregation procedure with the inferior information recovered by spatial or spectral mode (verified by the results comparing [26] with our method in experiment).

To overcome this limitation, we propose a simple yet effective unidirectional low-rank tensor recovery method, in which only the low-rank constraint along the non-local self-similarity direction is introduced, so as to reasonably capture the intrinsic sparsity configurations inside the constructed tensor. This is in line with the rule of Ockham's razor: "Entities must not be multiplied beyond necessity". Mathematically, given a constructed noisy tensor $\mathcal{X}_i \in$

$\mathbb{R}^{P^2 \times (K+1) \times B}$, we want to estimate the clean tensor $\mathcal{L}_i$ by solving the following problem:

$$\hat{\mathcal{L}}_i = \arg\min_{\mathcal{L}_i} \frac{1}{\lambda_i^2}||\mathcal{L}_i - \mathcal{X}_i||_F^2 + rank_2(\mathcal{L}_i), \quad (1)$$

where $rank_2(\mathcal{L}_i) = rank(\boldsymbol{L}_i^{(2)}) = \sum_j \left|\sigma_j(\boldsymbol{L}_i^{(2)})\right|_1$ [15, 8] is the sum of the singular values of the tensor unfold along the mode-2, $\sigma_j(\boldsymbol{L}_i^{(2)})$ means the j-th singular value of $\boldsymbol{L}_i^{(2)}$, λ_i^2 denotes the noise variance of the corresponding constructed tensor. Compared with conventional tensor sparsity measures, the proposed unidirectional low-rank constraint has two remarkable advantages. On one hand, it can more faithfully represent the structural correlation of the constructed tensor, leading to better denoising result. On the other hand, it significantly reduces the processing time by cutting down the unnecessary computation burden of the spatial and spectral low-rank constraint.

3.4. Hyper-Laplacian regularized low-rank tensor recovery model

Although the low-rank tensor recovery methods have achieved excellent results, they suffer from the common consistency issue of pixels in overlapped regions, namely the ring artifact [Fig. 3(c)], since they handled each cubic independently and averaged the overlapped pixels. The pioneer works, such as EPLL [35] and CSC [13] have been proposed to address the problem in single image.

The spatial and spectral information are the two sides of the same coin. In this paper, we solve this problem from the spectral sparsity perspective by enforcing an analysis-based hyper-Laplacian prior on the spectral gradient, so as to reduce the artifacts in spatial domain meanwhile to better preserve the spectral structure. As shown in Fig. 3(d), the result with hyper-Laplacian term is free from ring artifact.

Moreover, the spectral hyper-Laplacian prior could facilitate to faithfully preserve the intrinsic spectral structure. In Fig. 3(e), we have performed a statistical experiment on CAVE dataset to show that the empirically spectral gradient distribution (blue) is sparser than a Laplacian (purple) or Gaussian distribution (green), being well modeled by a hyper-Laplacian. In Fig. 3(f), the recovery spectral information (red) is more similar to the original one (green) compared with the non-hyper-Laplacian one (blue), which further validates the spectral geometric structure preserving ability of hyper-Laplacian term.

Thus, it is natural for us to incorporate both the unidirectional low-rank tensor (1) and hyper-Laplacian term into a whole image recovery model along with the constraint of linear measurements:

$$\left\{\hat{\mathcal{X}}, \hat{\mathcal{L}}_i\right\} = \arg\min_{\mathcal{X}, \mathcal{L}_i} \frac{1}{2}||\mathcal{X} - \mathcal{Y}||_F^2 + \mu||\nabla_z\mathcal{X}||_p$$
$$+ \omega \sum_i \left(\frac{1}{\lambda_i^2}||\mathcal{R}_i\mathcal{X} - \mathcal{L}_i||_F^2 + rank_2(\mathcal{L}_i)\right), \quad (2)$$

where $\mathcal{Y} \in \mathbb{R}^{M \times N \times B}$ is the noisy data, $\mathcal{R}_i \mathcal{X}$ represents the constructed tensor for each exemplar cubic, ∇_z denotes the first-order forward finite-difference operator along the z-axis (spectral direction), $p\,(0 \leq p \leq 1)$ is the parameter to control the sparsity of hyper-Laplacian, μ and ω are the regularization parameters. The basic idea of the model is that the intrinsic subspace of the non-local self-similarity cubics can be well depicted by the unidirectional low-rank tensor prior, and meanwhile the hyper-Laplacian regularizes the sparsity of spectral structure. This unified framework could benefit from the combination of synthesis-based low-rank prior and analysis-based hyper-Laplacian prior, yielding artifacts free result with faithful structure.

3.5. Optimization

Due to the difficulty of estimating multiple variables directly, we adopt the alternating minimization scheme to solve the objective functional (2) with respect to the whole image $\mathcal{X}$ and low-rank tensor $\mathcal{L}_i$ per each location.

3.5.1 Low-rank tensor estimation: $\mathcal{L}_i$

In this subproblem, we fix the other variable $\mathcal{X}$ and optimize the $\mathcal{L}_i$ by with its tensor unfolding formation

$$\hat{\boldsymbol{L}}_i^{(2)} = \arg\min_{\boldsymbol{L}_i^{(2)}} \frac{1}{\lambda_i^2} ||\boldsymbol{R}_i \boldsymbol{X}^{(2)} - \boldsymbol{L}_i^{(2)}||_F^2 + ||\boldsymbol{L}_i^{(2)}||_*, \quad (3)$$

where $\boldsymbol{R}_i \boldsymbol{X}^{(2)}$ corresponds to the matrix of the unfolding tensor $\mathcal{R}_i \mathcal{X}$ along the mode-2, $||\boldsymbol{L}_i^{(2)}||_*$ means the matrix nuclear norm to replace $rank(\boldsymbol{L}_i^{(2)})$ as its convex surrogate functional. Equation (3) is a typical low-rank matrix approximation problem which has a closed-form solution and can be easily solved by the singular values thresholding algorithm [1]. In our implementation, we borrow the idea of the reweighting strategy from [12] to improve the performance. After each $\boldsymbol{L}_i^{(2)}$ is obtained, the tensor folding is performed to transform them into 3-order tensors.

3.5.2 Image restoration: $\mathcal{X}$

We apply the alternative direction multiplier method [17] by introducing auxiliary variable so as to split the original complex problem into several easy subproblems.

$$\left\{\hat{\mathcal{X}}, \hat{\mathcal{D}}\right\} = \arg\min_{\mathcal{X}, \mathcal{D}} \mu||\mathcal{D}||_p + \frac{\alpha}{2}||\mathcal{D} - \nabla_z \mathcal{X} - \frac{\mathcal{J}}{\alpha}||_F^2$$
$$+ \frac{1}{2}||\mathcal{X} - \mathcal{Y}||_F^2 + \omega \sum_i \frac{1}{\lambda_i^2}||\mathcal{R}_i \mathcal{X} - \mathcal{L}_i||_F^2, \quad (4)$$

where $\mathcal{D} \in \mathbb{R}^{M \times N \times B}$ is an auxiliary variable, $\mathcal{J}$ is the Lagrangian multiplier, α and is a positive scalar.

1) **Update for $\mathcal{D}$: Hyper-Laplacian**. By ignoring terms independent of $\mathcal{D}$ in (4), we obtain following subproblem:

$$\hat{\mathcal{D}} = \arg\min_{\mathcal{D}} \mu||\mathcal{D}||_p + \frac{\alpha}{2}||\mathcal{D} - \nabla_z \mathcal{X} - \frac{\mathcal{J}}{\alpha}||_F^2, \quad (5)$$

which can be solved by conventional iteratively reweighted least squares or look-up table for specific values of p. In this work, we introduce the generalized iterated shrinkage algorithm [36] for non-convex ℓ_p-norm minimization (5), which is more efficient to implement, and converges to a more accurate solution.

2) **Update for $\mathcal{X}$: Restoration**. Similarly, dropping out the irrelevant variable in (4), we can get the following subproblem:

$$\hat{\mathcal{X}} = \arg\min_{\mathcal{X}} \frac{1}{2}||\mathcal{X} - \mathcal{Y}||_F^2 + \frac{\alpha}{2}||\mathcal{D} - \nabla_z \mathcal{X} - \frac{\mathcal{J}}{\alpha}||_F^2$$
$$+ \omega \sum_i \frac{1}{\lambda_i^2}||\mathcal{R}_i \mathcal{X} - \mathcal{L}_i||_F^2. \quad (6)$$

Generally, Eq. (6) is a quadratic optimization and can be solved by Gauss-Seidel algorithm. In this work, since the difference operator can be handled in Fourier transform very fast, we further introduce the ADMM for splitting Eq. (6) with subproblems that admit closed form solutions by the n-D fast Fourier transform. The details can be found in the supplementary material.

4. Experimental Results

4.1. Experimental setting

Our approach is compared with the comprehensive MSI denoising methods: 1-D sparse representation based methods (SDS [14], ANLM [20]), 2-D low-rank matrix recovery methods (LRMR [30], NMF [28]), state-of-the-art tensor methods (BM3D [5], LRTA [22], BM4D [18], TDL [21], ISTReg [26]). All the parameters are fine-tuned by default or following the rules in their papers to achieve the best performance. The Matlab code of proposed method can be downloaded at the author's homepage[2].

The spatial and spectral quality of the denoising results are very important for the subsequent processing, but is difficult to judge visually. In order to give an overall evaluation, four quantitative quality indices are employed: PSNR, SSIM, ERGAS [25], and SAM [29]. PSNR and SSIM are two conventional spatial-based indexes, while ERGAS and SAM are spectral-based evaluation indexes. The bigger PSNR and SSIM values are, and the smaller ERGAS and SAM values are, the better the restored images are.

We evaluate the competing methods on four representative datasets: Columbia Multispectral Database (CAVE)[3], Berkeley Segmentation Dataset (BSD)[4], Harvard real-world Hyperspectral Dataset (HHD)[5], and Airborne Visible/Infrared Imaging Spectrometer Dataset (AVIRIS)[6]. The CAVE and BSD are used for simulated experiments, while the HHD and AVIRIS are used to test the real cases.

---

[2]http://www.escience.cn/people/changyi/index.html
[3]http://www1.cs.columbia.edu/CAVE/databases/multispectral/
[4]https://www2.eecs.berkeley.edu/Research/Projects/CS/vision/bsds/
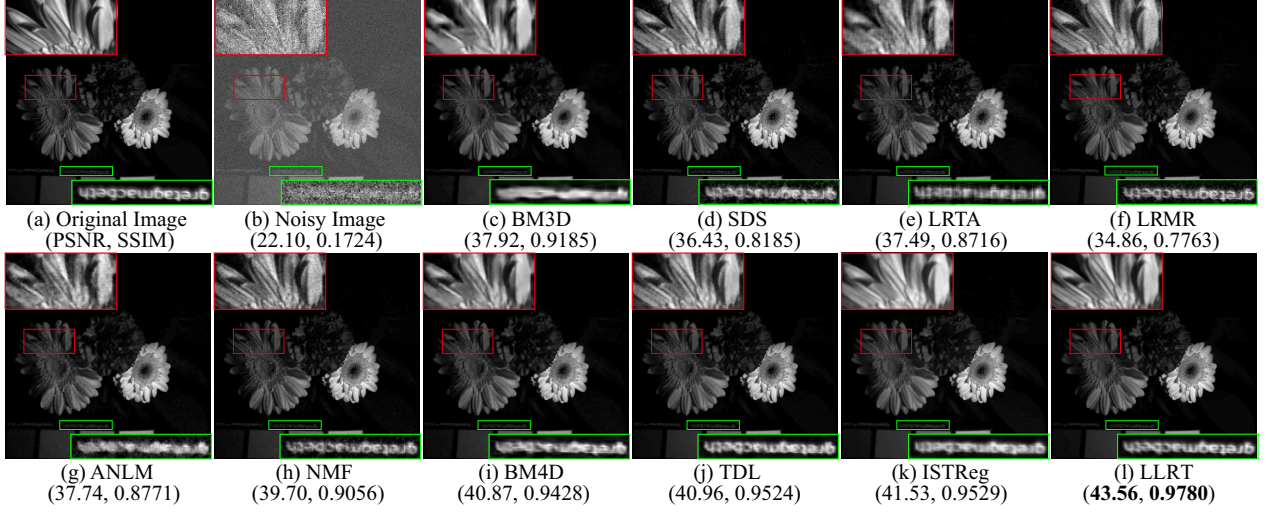[5]http://vision.seas.harvard.edu/hyperspec/index.html
[6]http://aviris.jpl.nasa.gov/data/

Figure 4. Simulated random noise removal results at 510nm band of image *Flower* under noise level $\lambda^2=20$ on CAVE dataset.

The figure shows subfigures labeled:
(a) Original Image (PSNR, SSIM)
(b) Noisy Image (22.10, 0.1724)
(c) BM3D (37.92, 0.9185)
(d) SDS (36.43, 0.8185)
(e) LRTA (37.49, 0.8716)
(f) LRMR (34.86, 0.7763)
(g) ANLM (37.74, 0.8771)
(h) NMF (39.70, 0.9056)
(i) BM4D (40.87, 0.9428)
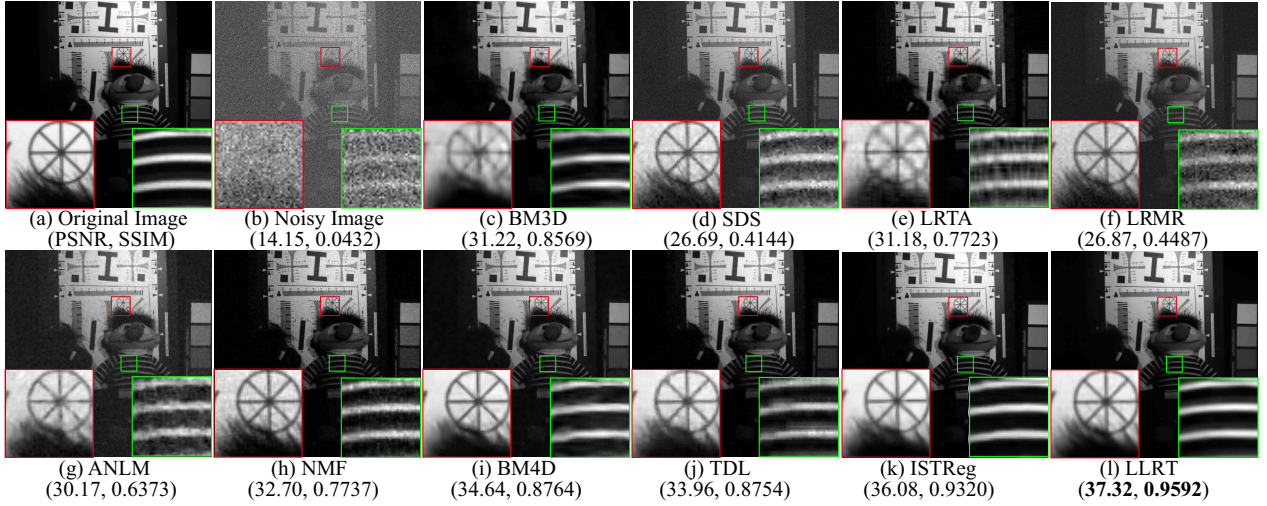(j) TDL (40.96, 0.9524)
(k) ISTReg (41.53, 0.9529)
(l) LLRT (**43.56**, **0.9780**)

Figure 5. Simulated random noise removal results at 510nm band of image *Toy* under noise level $\lambda^2=50$ on CAVE dataset.

The figure shows subfigures labeled:
(a) Original Image (PSNR, SSIM)
(b) Noisy Image (14.15, 0.0432)
(c) BM3D (31.22, 0.8569)
(d) SDS (26.69, 0.4144)
(e) LRTA (31.18, 0.7723)
(f) LRMR (26.87, 0.4487)
(g) ANLM (30.17, 0.6373)
(h) NMF (32.70, 0.7737)
(i) BM4D (34.64, 0.8764)
(j) TDL (33.96, 0.8754)
(k) ISTReg (36.08, 0.9320)
(l) LLRT (**37.32**, **0.9592**)

4.2. Experimental results

Zero mean additive white Gaussian noises with difference variance are added to generate the noisy observations. The visual results of single band in CAVE *Flower* and *Toy* under different noise level are shown in Figs. 4 and 5, respectively. Results on more noise levels can be found in the supplementary material. Compared with other methods, the LLRT exhibits more clear details in texture regions or edges, meanwhile produce clean results in smooth regions with higher PSNR values. The overall quantitative assessment results by the competing denoising methods are shown in Table 1. The LLRT achieves the best performance in all quantitative assessments. Moreover, with the increasing of noise level, the advantage of LLRT over other methods be-

comes bigger by a large marginal.

We show that multi-band images such as RGB images also benefit from our method. We compare the proposed method with WNNM [12], which handles the color image in each channel, and state-of-the-art color image denoising methods, such as LSCD [23], color BM3D (CBM3D) [4]. The visual result of color image *Mushroom* on BSD under noise level $\lambda^2=40$ are shown in Fig. 6. The quantitative assessment results are shown in Table 2. Compared with other competing methods, the proposed method could better preserve the image details with less chrominance color artifacts and highest PSNR values.

To demonstrate the robustness of our method, we show in Fig. 7 a real AVIRIS image denoising result. It is shown that the proposed method clearly outperformed the com-

Table 1. Quantitative results of different methods under several noise levels on CAVE dataset.

Sigma	Index	Methods										
		Noisy	BM3D [5]	SDS [14]	LRTA [22]	LRMR [30]	ANLM [20]	NMF [28]	BM4D [18]	TDL [21]	ISTReg [26]	LLRT
10	PSNR	28.13	42.09	39.74	41.36	39.27	41.52	43.15	44.59	44.30	45.77	**46.67**
	SSIM	0.4371	0.9665	0.9484	0.9499	0.9094	0.9576	0.9702	0.9784	0.9797	0.9802	**0.9872**
	ERGAS	236.40	45.06	61.86	49.53	64.81	47.78	39.65	33.33	34.86	30.53	**26.74**
	SAM	0.7199	0.1395	0.2160	0.1719	0.3343	0.2184	0.1358	0.1295	0.1025	0.1086	**0.0841**
30	PSNR	18.59	36.40	32.10	36.15	31.36	34.77	36.53	38.90	39.03	40.51	**41.55**
	SSIM	0.0988	0.9034	0.6709	0.8787	0.6451	0.8060	0.8565	0.9277	0.9486	0.9488	**0.9683**
	ERGAS	709.29	88.29	145.88	91.40	157.65	104.95	86.25	65.38	63.54	53.05	**48.20**
	SAM	1.0414	0.2489	0.5050	0.2479	0.6021	0.4376	0.2465	0.2598	0.1520	0.1374	**0.1192**
50	PSNR	14.15	32.66	25.32	32.44	26.67	30.74	31.98	35.96	36.42	37.75	**38.93**
	SSIM	0.0432	0.8320	0.3451	0.7932	0.4000	0.6057	0.7113	0.8666	0.9175	0.9271	**0.9521**
	ERGAS	1181.95	115.06	280.88	118.64	264.28	164.55	123.23	91.51	85.58	70.16	**65.52**
	SAM	1.1741	0.2877	0.7006	0.2843	0.7534	0.5806	0.3148	0.3575	0.2000	0.1619	**0.1424**
100	PSNR	8.13	29.27	17.90	29.20	20.84	24.90	26.95	30.82	32.91	33.01	**35.40**
	SSIM	0.0122	0.7460	0.1047	0.6945	0.1850	0.2826	0.4643	0.6956	0.8344	0.8648	**0.9143**
	ERGAS	2364.05	171.94	693.94	175.91	469.26	324.48	225.55	141.18	128.22	120.77	**98.91**
	SAM	1.3271	0.3938	0.9690	0.3381	0.9306	0.7972	0.4321	0.5014	0.3079	0.2376	**0.1895**

(a) Original (PSNR:dB) (b) Noisy (16.09) (c) WNNM (26.99) (d) LSCD (27.17) (e) CBM3D (28.03) (f) LLRT (**28.32**)
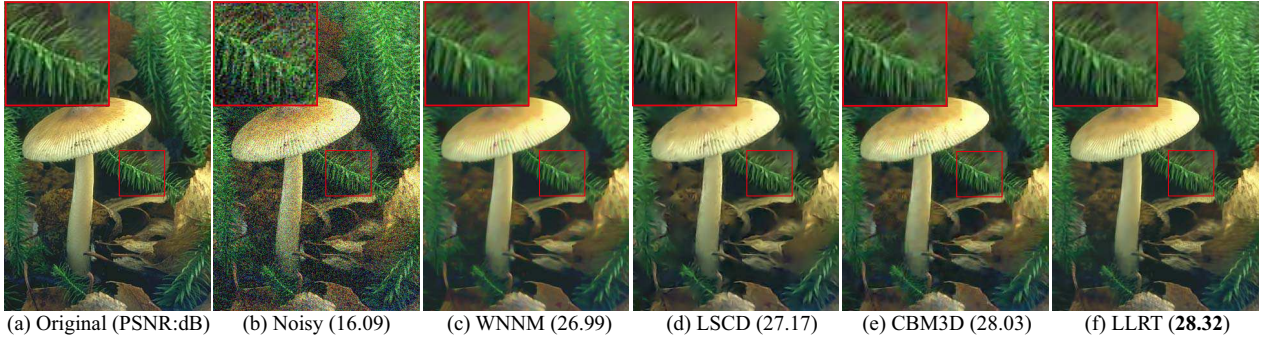
Figure 6. Simulated color image *mushroom* results under noise level $\lambda^2{=}40$ on BSD dataset.

Table 2. Quantitative results of different methods under several noise levels on BSD.

Sigma	Index	Methods			
		Noisy	LSCD [23]	CBM3D [4]	LLRT
10	PSNR	28.13	33.85	35.90	**36.04**
	SSIM	0.7020	0.9188	0.9501	**0.9513**
20	PSNR	22.17	30.26	31.85	**32.00**
	SSIM	0.4580	0.8469	0.8923	**0.8957**
30	PSNR	18.58	28.22	29.69	**29.87**
	SSIM	0.3223	0.7854	0.8402	**0.8434**
40	PSNR	16.08	27.00	28.10	**28.50**
	SSIM	0.2388	0.7417	0.7872	**0.7992**

Figure 8. Effects of the numbers of bands and non-local cubics on denoising results.

pared methods with better visual appearance and less visual artifacts. From the demarcated window, we can observe that the proposed method obtains clean image with abundant edge structures.

4.3. Analysis and Discussion

Parameter setting. For the proposed method, the number of the bands B and non-local cubics K are two important parameters. In Fig. 8, we show the changes of the PSNR and SSIM values in CAVE with the different numbers of B and K, respectively. It is observed the denoising results gradually become better with larger number of bands and non-local cubics, and trend toward steady. We empirically set $K \in [200, 400]$, $B \in [20, 40]$, and fix others $p = 0.5$,

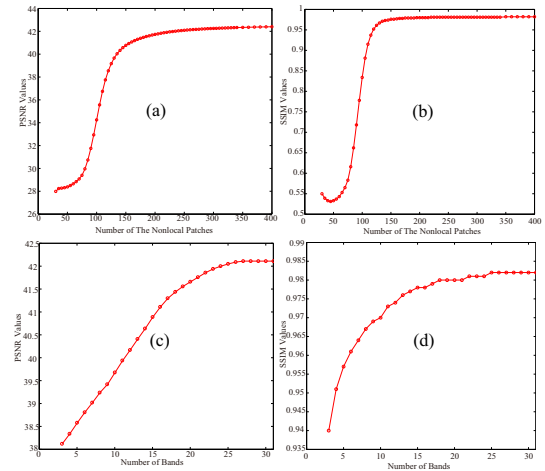$\mu = 0.8$, $\omega = 1$ in all experiments.

Robustness to band inconsistency. Most of the low-rank based methods rely on the assumption that the spectral mode lie on the low-rank subspace, which may be violated in real images [3]. To illustrate this, in Fig. 9, we show the results of LRMR (a representative method utilizing spec-
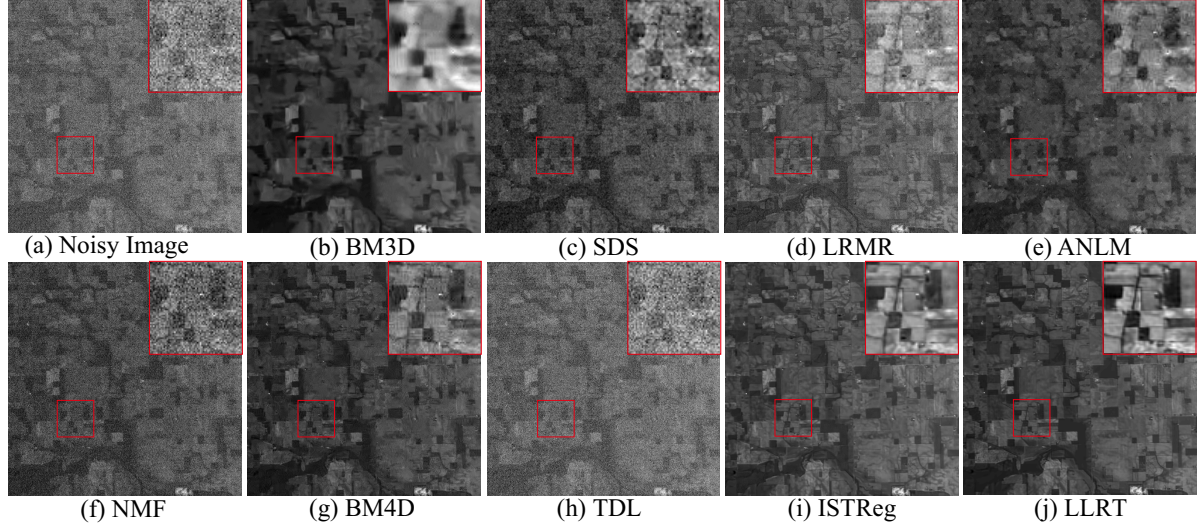
(a) Noisy Image   (b) BM3D   (c) SDS   (d) LRMR   (e) ANLM

(f) NMF   (g) BM4D   (h) TDL   (i) ISTReg   (j) LLRT

Figure 7. Real random noise removal results on AVIRIS dataset.
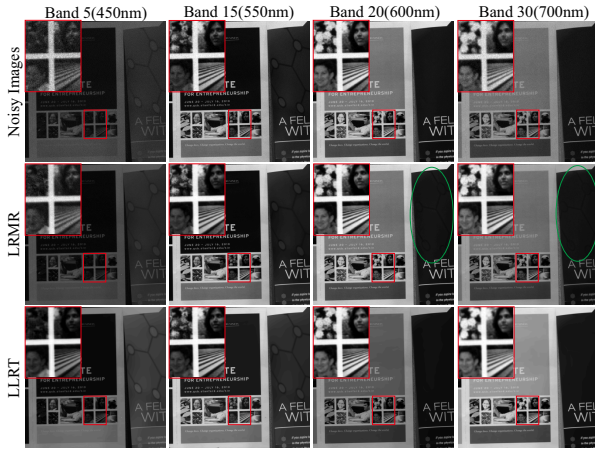
Figure 9. The robustness of LLRT method under the band inconsistency situation.

Table 3. Running time comparison (In seconds)

size	TDL[21]	LRMR[30]	RLRTR[16]	ISTReg[26]	LLRT
512*512*31	61	303	2646	2103	1093

local similarity cubic matching, we propose to average each band of the cubic, which can be regarded as a uniform filtering procedure. Matching processing is performed on the "clean" 2-D matrix which could significantly reduce computational load and improve matching accuracy. The k-mean++ introduced by TDL [21] excellently speeds up the non-local patch searching, making it much faster than that of the others. For the optimization procedure, we split the original problem into several subproblems with closed-form solution, either via n-D FFT or fast shrinkage operation, which requires only a few operations per element.

5. Conclusion

As the proverb goes, every advantage has its disadvantage. The spatial and spectral information in MSI offer abundant structure correlations, while the processing time increases rapidly. Based on the analysis of the structure correlations in MSI and their effects on denoising performance, we have proposed a simple yet effective hyper-Laplacian regularized unidirectional low-rank tensor recovery method that not only truthfully represents the structure correlation but also reduces the processing time. Moreover, the global hyper-Laplacian prior is introduced to avoid the consistency issue from the spectral smoothness perspective. The proposed method has been tested on several MSI datasets, and it consistently outperformed the competing approaches.

tral low-rank assumption) on a HHD image, in which the original image of different band varies slowly. In the second row, the LRMR introduces the spectral distortion artifact, namely false edge structure marked in the green ellipse. As for the result of proposed method, not only the random noise is removed satisfactorily, but also the different structural edges of each frame has been preserved well.

Computational efficiency. In Table 3, we compare the computational efficiency with the other low-rank matrix/tensor algorithms: TDL [21], LRMR [30], RLRTR [16], ISTReg [26]. Our method is faster than the tensor-based low-rank methods, such as RLRTR, ISTReg. The non-local self-similarity searching and optimization procedure contribute most of the processing time. For the non-

References

[1] J.-F. Cai, E. J. Candès, and Z. Shen. A singular value thresholding algorithm for matrix completion. *SIAM J. on Optim.*, 20(4):1956–1982, 2010.

[2] E. J. Candès, M. B. Wakin, and S. P. Boyd. Enhancing sparsity by reweighted ℓ_1 minimization. *J. Fourier Anal. Appl.*, 14(5-6):877–905, 2008.

[3] Y. Chang, L. Yan, H. Fang, and C. Luo. Anisotropic spectral-spatial total variation model for multispectral remote sensing image destriping. *IEEE TIP*, 24(6):1852–1866, 2015.

[4] K. Dabov, A. Foi, V. Katkovnik, and K. Egiazarian. Color image denoising via sparse 3d collaborative filtering with grouping constraint in luminance-chrominance space. In *ICIP*, pages I–313, 2007.

[5] K. Dabov, A. Foi, V. Katkovnik, and K. Egiazarian. Image denoising by sparse 3-d transform-domain collaborative filtering. *IEEE Trans. Image Process.*, 16(8):2080–2095, 2007.

[6] W. Dong, F. Fu, G. Shi, X. Cao, J. Wu, G. Li, and X. Li. Hyperspectral image super-resolution via non-negative structured sparse representation. *IEEE Trans. Image Process.*, 25(5):2337–2352, 2016.

[7] W. Dong, G. Li, G. Shi, X. Li, and Y. Ma. Low-rank tensor approximation with laplacian scale mixture modeling for multiframe image denoising. In *ICCV*, pages 442–449, 2015.

[8] M. Fazel. *Matrix rank minimization with applications*. PhD thesis, PhD thesis, Stanford University, 2002.

[9] Y. Fu and W. Dong. 3d magnetic resonance image denoising using low-rank tensor approximation. *Neurocomputing*, 195:30–39, 2016.

[10] Y. Fu, A. Lam, I. Sato, and Y. Sato. Adaptive spatial-spectral dictionary learning for hyperspectral image denoising. In *ICCV*, pages 343–351, 2015.

[11] Y. Fu, Y. Zheng, I. Sato, and Y. Sato. Exploiting spectral-spatial correlation for coded hyperspectral image restoration. In *CVPR*, pages 3727–3736, 2016.

[12] S. Gu, L. Zhang, W. Zuo, and X. Feng. Weighted nuclear norm minimization with application to image denoising. In *CVPR*, pages 2862–2869, 2014.

[13] S. Gu, W. Zuo, Q. Xie, D. Meng, X. Feng, and L. Zhang. Convolutional sparse coding for image super-resolution. In *ICCV*, pages 1823–1831, 2015.

[14] A. Lam, I. Sato, and Y. Sato. Denoising hyperspectral images using spectral domain statistics. In *ICPR*, pages 477–480, 2012.

[15] L. D. Lathauwer, B. D. Moor, and J. Vandewalle. A multilinear singular value decomposition. *SIAM J. Matrix Anal. Appl.*, 21(4):1253–1278, 2000.

[16] C. Li, Y. Ma, J. Huang, X. Mei, and J. Ma. Hyperspectral image denoising using the robust low-rank tensor recovery. *JOSA A*, 32(9):1604–1612, 2015.

[17] Z. Lin, R. Liu, and Z. Su. Linearized alternating direction method with adaptive penalty for low-rank representation. In *NIPS*, pages 612–620, 2011.

[18] M. Maggioni, V. Katkovnik, K. Egiazarian, and A. Foi. Nonlocal transform-domain filter for volumetric data denoising and reconstruction. *IEEE Trans. Image Process.*, 22(1):119–33, 2012.

[19] J. Mairal, F. Bach, J. Ponce, G. Sapiro, and A. Zisserman. Non-local sparse models for image restoration. In *ICCV*, pages 2272–2279, 2009.

[20] J. V. Manjón, P. Coupé, L. Martí-Bonmatí, D. L. Collins, and M. Robles. Adaptive non-local means denoising of mr images with spatially varying noise levels. *J. Magn. Resonance Imag.*, 31(1):192–203, 2010.

[21] Y. Peng, D. Meng, Z. Xu, C. Gao, Y. Yang, and B. Zhang. Decomposable nonlocal tensor dictionary learning for multispectral image denoising. In *CVPR*, pages 2949–2956, 2014.

[22] N. Renard, S. Bourennane, and J. Blanc-Talon. Denoising and dimensionality reduction using multilinear tools for hyperspectral images. *IEEE Geosci. Remote Sens. Lett.*, 5(2):138–142, 2008.

[23] M. Rizkinia, T. Baba, K. Shirai, and M. Okuda. Local spectral component decomposition for multi-channel image denoising. *IEEE Trans. Image Process.*, 25(7):3208–3218, 2016.

[24] B. Romera-Paredes and M. Pontil. A new convex relaxation for tensor completion. In *NIPS*, pages 2967–2975, 2013.

[25] L. Wald. *Data fusion: definitions and architectures: fusion of images of different spatial resolutions*. Presses des MINES, 2002.

[26] Q. Xie, Q. Zhao, D. Meng, Z. Xu, S. Gu, W. Zuo, and L. Zhang. Multispectral images denoising by intrinsic tensor sparsity regularization. In *CVPR*, pages 1692–1700, 2016.

[27] Y. Xie, Y. Qu, D. Tao, W. Wu, Q. Yuan, and W. Zhang. Hyperspectral image restoration via iteratively regularized weighted schatten-norm minimization. *IEEE Trans. Geosci. Remote Sens.*, 54(8):4642–4659, 2016.

[28] M. Ye, Y. Qian, and J. Zhou. Multitask sparse nonnegative matrix factorization for joint spectral–spatial hyperspectral imagery denoising. *IEEE Trans. Geosci. Remote Sens.*, 53(5):2621–2639, 2015.

[29] R. H. Yuhas, J. W. Boardman, and A. F. Goetz. Determination of semi-arid landscape endmembers and seasonal trends using convex geometry spectral unmixing techniques. In *Summaries of the 4th Annual JPL Airborne Geoscience Workshop*, 1993.

[30] H. Zhang, W. He, L. Zhang, H. Shen, and Q. Yuan. Hyperspectral image restoration using low-rank matrix recovery. *IEEE Trans. Geosci. Remote Sens.*, 52(8):4729–4743, 2014.

[31] L. Zhang, W. Wei, Y. Zhang, F. Li, C. Shen, and Q. Shi. Hyperspectral compressive sensing using manifold-structured sparsity prior. In *ICCV*, pages 3550–3558, 2015.

[32] L. Zhang, W. Wei, Y. Zhang, C. Shen, A. van den Hengel, and Q. Shi. Cluster sparsity field for hyperspectral imagery denoising. In *ECCV*, pages 631–647, 2016.

[33] J. Zhao, Y. Zhong, H. Shu, and L. Zhang. High-resolution image classification integrating spectral-spatial-location cues by conditional random fields. *IEEE Trans. Image Process.*, 25(9):4033–4045, 2016.

[34] Q. Zhao, D. Meng, X. Kong, Q. Xie, W. Cao, Y. Wang, and Z. Xu. A novel sparsity measure for tensor recovery. In *ICCV*, pages 271–279, 2015.

[35] D. Zoran and Y. Weiss. From learning models of natural image patches to whole image restoration. In *ICCV*, pages 479–486, 2011.

[36] W. Zuo, D. Meng, L. Zhang, X. Feng, and D. Zhang. A generalized iterated shrinkage algorithm for non-convex sparse coding. In *ICCV*, pages 217–224, 2013.